

# Effect of surfactants on the stability of two-layer channel flow

By M. G. BLYTH<sup>1</sup> AND C. POZRIKIDIS<sup>2</sup>

<sup>1</sup>School of Mathematics, University of East Anglia, Norwich, NR4 7TJ, UK  
M.Blyth@uea.ac.uk

<sup>2</sup>Department of Mechanical and Aerospace Engineering, University of California,  
San Diego, La Jolla, CA 92093-0411, USA  
cpozrikidis@ucsd.edu

(Received 31 January 2003 and in revised form 28 October 2003)

The effect of an insoluble surfactant on the stability of two-layer viscous flow in an inclined channel confined by two parallel walls is considered. A lubrication-flow model applicable to long waves and low-Reynolds-number-flow is developed, and pertinent nonlinear evolution equations for the interface position and surfactant concentration are derived. Linear stability analysis based on the lubrication-flow model and the inclusive equations of Stokes flow confirm the recent findings of Frenkel & Halpern (2002) and Halpern & Frenkel (2003) that the presence of an insoluble surfactant induces a Marangoni instability in certain regions of parameter space defined by the layer thickness and viscosity ratios. Numerical simulations based on both approaches show that the interfacial waves may grow and saturate into steep profiles. The lubrication-flow model is adequate in capturing the essential features of the instability for small and moderate wavenumbers.

---

## 1. Introduction

Frenkel & Halpern (2002) and Halpern & Frenkel (2003) recently discovered that the presence of an insoluble surfactant on a sheared interface induces a Marangoni instability even in the absence of fluid inertia. In particular, they demonstrated that a quiescent interface may become unstable as soon as it is subjected to a local shear flow due to periodic accumulation of surfactant and accompanying spatial variations in surface tension. In the first part of their work, Frenkel & Halpern (2002) carried out a linear stability analysis of two-layer Couette–Poiseuille channel flow, considering the limit of long waves and vanishing Reynolds number. Subsequently, Halpern & Frenkel (2003) extended the analysis to perturbations of arbitrary wavelength, and identified the regions of instability in parameter space consisting of the layer thickness and viscosity ratio, under the assumption of Stokes flow.

Halpern and Frenkel's work can be regarded as an extension of Yih's (1967) classical analysis on the interfacial instability of parallel flow due to viscosity stratification in the absence of surfactants. Yih and subsequent authors demonstrated that, when the fluids are neutrally or stably stratified, instability occurs only at non-zero Reynolds numbers, however small (e.g. Pozrikidis 1997*a*, 1998*a*, 2004). One important difference between Frenkel & Halpern's Marangoni instability and Yih's instability is that in the former waves grow even under conditions of Stokes flow. Moreover, increasing the viscosity contrast does not necessarily amplify the growth rates.

In related work, *Thaokar & Kumaran (2002)* considered the Couette flow of two layers in a channel, where the fluids are separated by a thin, impermeable elastic membrane. The interface develops elastic tensions according to the local membrane strain, and viscous tensions according to the local rate of deformation. By carrying out both a linear and weakly nonlinear analysis, the authors showed that, in the limit of zero Reynolds number, the initially flat interface loses stability to growing modes with small wavenumbers. In this problem, the spatial variation in the interfacial tension is due to the elastic properties of the membrane rather than to changes induced in the local surface tension by the presence of a surfactant. The mechanism for instability is therefore somewhat different than the one associated with the Marangoni instability.

The findings of *Frenkel & Halpern (2002)* and *Halpern & Frenkel (2003)* put the spotlight on a physical situation where the normally stabilizing action of a surfactant may have an adverse effect. Although surfactant hydrodynamics has been discussed extensively in the literature both from a fundamental and an applied point of view, the broad implications of a surfactant-induced instability do not seem to have been fully appreciated. Indeed, it is generally accepted that surfactants have a stabilizing influence on interfacial shapes in the presence or absence of a base flow. The underlying reasoning is that surfactants lower the surface tension and thereby diminish the intensity of capillary forces causing interfacial distortion. Thus, surfactants are added to the biological film coating on the inside of a cylindrical tube, such as the mucus lining the bronchioles, to delay the onset of a Rayleigh capillary instability leading to airway closure.

A consequence of lowering the surface tension by the use of surfactants is the development of surface tension gradients and accompanying Marangoni tractions. Evidence for the possible destabilizing influence of the latter is available directly from the recent analysis of *Frenkel and Halpern*, and indirectly from stability analysis of gravity-driven film flow. Regarding the latter, *Ji & Setterwall (1994)* studied the stability of film flow down a plane wall including the effect of a soluble surfactant, and discovered the existence of an unstable normal mode related to Marangoni tractions at low Reynolds numbers and for moderate- and short-wavelength perturbations. More recently, *Pozrikidis (2003)* studied the stability of a film down an inclined plane in the presence of an insoluble surfactant in Stokes flow, and identified a Marangoni normal mode whose rate of decay is lower than that of the usual mode for a clean free surface. It is possible then that inertial effects will first destabilize this mode, effectively lowering the threshold Reynolds number for stable unidirectional motion.

In this paper, we reconsider the influence of an insoluble surfactant on the interfacial stability of two-layer channel flow, with several objectives: to confirm the instability discovered by *Frenkel and Halpern*, to generalize the linear stability analysis by including the effect of gravity and surfactant surface diffusivity, to develop a lubrication-flow model applicable to long waves, to describe the properties of the normal modes and thus provide a physical reasoning for the onset of the Marangoni instability, and finally to illustrate the nonlinear dynamics of the finite-amplitude motion in the limit of vanishing Reynolds numbers. Numerical simulations are conducted using both the lubrication-flow model and the boundary-element method for Stokes flow.

The linearized analysis is first performed for arbitrary wavenumbers, with the linear growth rates being computed exactly, and then under the auspices of the lubrication approximation applicable to small wavenumbers. Our approach in the second case differs from that of *Frenkel & Halpern (2002)* in that the evolution equations are derived by linearizing the lubrication-flow model instead of introducing wavenumber

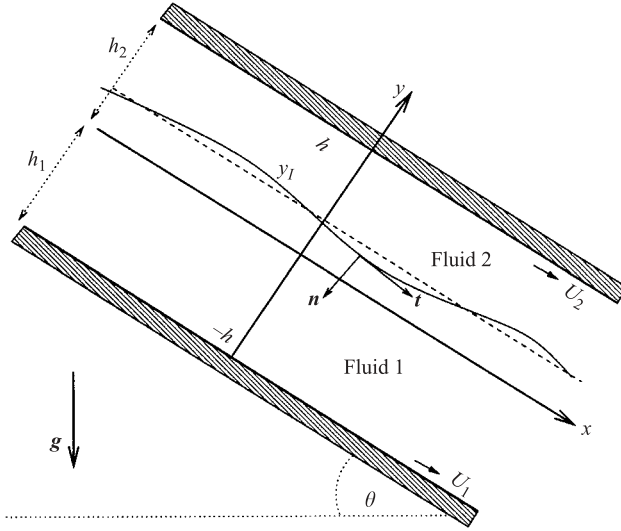


FIGURE 1. Definition sketch of two-layer flow in a channel, showing the position of the unperturbed and perturbed interface described by  $y = y_l(x, t)$ ; the unperturbed interface is drawn with the broken line. The unit normal to the interface,  $\mathbf{n}$ , points into the lower fluid labelled 1; the unit tangent,  $\mathbf{t}$ , points in the direction of increasing arc length  $l$ . The lower and upper walls are free to move parallel to themselves with velocities  $U_1$  and  $U_2$ .

expansions in the Orr–Sommerfeld equation for Stokes flow. The range of validity of the approximate results for long waves will be assessed, and the veracity of both analyses will be confirmed by comparison with numerical solutions of the governing equations for small-amplitude perturbations.

We shall present numerical simulations that extend the linear stability analysis into the regime of finite-amplitude motion. The model equations derived under the long-wave approximation are solved using explicit time-marching finite-difference methods, while those for Stokes flow are solved by means of a boundary-integral technique combined with a finite-volume method for integrating the surfactant transport equation. The consistency of the results obtained by the lubrication-flow model and the boundary-integral solution will validate both approaches and corroborate the accuracy of the former as a simple means of describing the evolution under relevant flow conditions. The results will suggest that, under certain conditions, the instability saturates, leading to a disturbance wave of fixed amplitude, while overturning occurs under other conditions.

In §2, we pose the physical problem, state the governing equations, and identify dimensionless parameters determining the instability. In §3, we develop the lubrication-flow model and study the linear and nonlinear dynamics of the long-wave motion. In §4, we compare the growth rates predicted by the lubrication-flow model with those arising from the linear stability analysis for Stokes flow, and in §5, we discuss the results of numerical simulations based on the boundary-element method. Appendix A contains an outline of the stability analysis for Stokes flow, and Appendix B a brief description of the boundary-element method.

## 2. Problem statement

We consider the unidirectional flow of two superimposed viscous layers in an inclined channel that is confined by two parallel walls, as shown in figure 1. The

lower fluid is denoted by the subscript 1, and the upper fluid by the subscript 2. The motion may be driven by the translation of one or both walls, by gravity, by an imposed streamwise pressure gradient, or by a combination thereof. The interface is populated with an insoluble surfactant that is convected while diffusing over the interface to alter the surface tension  $\gamma$  in a way that is determined by an appropriate surface equation of state, to be discussed in §2.1.

At the interface, the hydrodynamic traction undergoes a jump in both the normal and tangential directions as a result of variations in surface tension. In particular, a tangential jump occurs because of the spatial variation in the interfacial surfactant concentration,  $\Gamma$ , which is responsible for the development of Marangoni tractions. Our main objective is to study the stability of the flow by examining the evolution of periodic waves in the limit of vanishing Reynolds number.

### 2.1. Surface equation of state

When the surfactant concentration is well below the saturation level, a linear relationship may be assumed between the surface tension and the surfactant concentration according to Gibbs' law,  $\gamma_c - \gamma = \Gamma RT$ , where  $R$  is the ideal gas constant,  $T$  is the absolute temperature, and  $\gamma_c$  is the surface tension of a clean interface which is devoid of surfactants (e.g. Adamson 1990; Pozrikidis 2004). Rearranging, we obtain the linear surface equation of state

$$\gamma = \gamma_c \left( 1 - \beta \frac{\Gamma}{\Gamma_0} \right), \quad (2.1)$$

where  $\beta = \Gamma_0 RT / \gamma_c$  is a dimensionless coefficient related to the surface elasticity by  $E = \gamma_c \beta / \Gamma_0$ , and  $\Gamma_0$  is a reference surfactant concentration corresponding to the surface tension  $\gamma_0 = \gamma_c (1 - \beta)$ . The importance of the surfactant for the interfacial dynamics is encapsulated in the dimensionless Marangoni number

$$Ma \equiv \frac{E \Gamma_0}{\gamma_0} = \frac{\beta}{1 - \beta}, \quad (2.2)$$

defined such that  $\partial\gamma/\partial\Gamma = -Ma\gamma_0/\Gamma_0$ . This relation and the linear law (2.1) may also be used to describe small perturbations from the base concentration,  $\Gamma_0$ , with the understanding that the Marangoni number and associated coefficient  $\beta$  are no longer physiochemical constants but express instead the surface elasticity pertinent to the current conditions.

### 2.2. Surfactant transport

The evolution of the surfactant concentration is governed by the convection–diffusion equation

$$\frac{d\Gamma}{dt} + \frac{\partial(u_t \Gamma)}{\partial l} - w \frac{\partial\Gamma}{\partial l} = -\Gamma \kappa u_n + D_s \frac{\partial^2 \Gamma}{\partial l^2}, \quad (2.3)$$

where  $u_t = \mathbf{u} \cdot \mathbf{t}$  and  $u_n = \mathbf{u} \cdot \mathbf{n}$  are the interfacial velocities in the directions of the tangential and normal vectors, respectively. With reference to figure 1,  $\kappa = -\mathbf{n} \cdot d\mathbf{t}/dl$  is the interfacial curvature in the  $(x, y)$ -plane,  $l$  is the arc length increasing in the direction of the unit tangent vector  $\mathbf{t}$ , and  $D_s$  is the surface surfactant diffusivity (e.g. Wong, Rumschitzki & Maldarelli 1996; Li & Pozrikidis 1997; Yon & Pozrikidis 1998). The derivative  $d/dt$  on the left-hand side of (2.3) expresses the rate of change of a variable following the motion of interfacial nodes moving with the component of the fluid velocity normal to the interface and with an arbitrary tangential velocity  $w(l)$ .

For example, if  $w = 0$ , the nodes are marker points moving normal to the interface, whereas if  $w = u_t$  the nodes are Lagrangian point particles moving with the local fluid velocity. In the case of steady flow, and when  $w = 0$ , the first terms on the left- and right-hand sides of (2.3) vanish, and the resulting equation expresses a balance between interfacial convection and diffusion along the stationary interface.

### 2.3. Stability of the unidirectional flow

Dimensional analysis reveals that the stability of the base unidirectional flow with a uniform surfactant concentration,  $\Gamma_0$ , corresponding to the surface tension,  $\gamma_0$ , is determined by seven parameters: the channel inclination angle,  $\theta_0$ , the viscosity ratio,  $\lambda = \mu_2/\mu_1$ , the density ratio,  $\delta = \rho_2/\rho_1$ , the Marangoni number defined in (2.2), and the capillary, Bond, and Péclet numbers

$$Ca = \frac{\xi_1 h \mu_1}{\gamma_0}, \quad Bo = \frac{h^2 \rho_1 |1 - \delta| g}{\gamma_0}, \quad Pe = \frac{\xi_1 h^2}{D_s}. \quad (2.4)$$

In the definition of the capillary and Péclet numbers,  $\xi_1$  is the shear rate of the base flow in the lower fluid evaluated at the position of the unperturbed interface.

## 3. Evolution of long waves

The evolution of long waves can be described efficiently working under the lubrication approximation. The main assumption is that appreciable streamwise variations in the flow variables occur on a length scale that is much larger than the channel width. Under these conditions, the Navier–Stokes equation is greatly simplified by assuming that the fluids are in a state of nearly unidirectional motion. The lubrication-flow model developed in this section is a generalization of the earlier models of Ooms *et al.* (1985) and Pozrikidis (1998a), the new feature being the presence of an insoluble surfactant.

### 3.1. Formulation

Integrating the  $x$  and  $y$  components of the equation of motion describing nearly unidirectional flow, we find the parabolic velocity profile and associated pressure field

$$\left. \begin{aligned} u^{(j)} &= -\frac{\chi_j + \rho_j g_x}{2\mu_j} (y - y_I)^2 + \xi_j (y - y_I) + u_I, \\ p^{(j)} &= -\int_{x_0}^x \chi_j(\eta, t) d\eta + \rho_j g_y y + P_j, \end{aligned} \right\} \quad (3.1)$$

where  $j = 1, 2$  denotes the lower and upper fluid ( $j = 1$  for  $-h < y < y_I(x, t)$ , and  $j = 2$  for  $y_I(x, t) < y < h$ ),  $x_0$  is an arbitrary reference point,  $u_I(x, t)$  is the local interfacial velocity, and  $P_j$  are constants. The functions  $\xi_1(x, t)$  and  $\xi_2(x, t)$  are the shear rates of the lower and upper fluid evaluated at the interface, while the functions  $\chi_j(x, t) \equiv -\partial p^{(j)}/\partial x$  express the negative of the streamwise pressure gradient within each layer. In the inclined system of coordinates employed here, the components of the acceleration due to gravity are  $g_x = g \sin \theta$  and  $g_y = -g \cos \theta$ . Though not involved in the lubrication-flow model, the  $y$  velocity component at the interface,  $v_I(x, t)$ , can be computed from the kinematic condition  $D[y_I(x, t) - y]/Dt = 0$ , where  $D/Dt$  is the material derivative, yielding  $v_I = \partial y_I/\partial t + u_I \partial y_I/\partial x$ . The  $y$  velocity profile can be found by integrating the continuity equation.

Requiring the no-slip boundary condition at the walls, we set  $u^{(1)}(y = -h) = U_1$  and  $u^{(2)}(y = h) = U_2$  to find

$$\xi_j = \pm \left[ -(\chi_j + \rho_j g_x) \frac{h_j}{2\mu_j} + \frac{u_I - U_j}{h_j} \right], \quad (3.2)$$

where the plus (minus) sign applies for the lower (upper) layer,  $j = 1$  (2), and

$$h_1(x, t) = h + y_I(x, t), \quad h_2(x, t) = h - y_I(x, t) \quad (3.3)$$

are the layer thicknesses. At the interface, the shear rates must satisfy the condition

$$\mu_1 \xi_1(x, t) = \mu_2 \xi_2(x, t) + \frac{\partial \gamma}{\partial x}, \quad (3.4)$$

where  $\gamma$  is the surface tension, and the final term represents the Marangoni traction. Substituting (3.2) and rearranging, we obtain the following expression for the interfacial velocity:

$$u_I = \frac{2h^2}{\mu_1} \frac{r}{(1+r)^2(\lambda+r)} \left\{ \chi_1 + \chi_2 r + \rho_1 g_x (1 + \delta r) + 2 \frac{\partial \gamma}{\partial x} \right\} + \frac{rU_1 + \lambda U_2}{\lambda + r}, \quad (3.5)$$

where  $r = h_2(x, t)/h_1(x, t)$  is the local instantaneous layer thickness ratio.

The normal stress is discontinuous at the interface due to surface tension. Under the lubrication approximation, the viscous contribution may be neglected, and the balance of normal stress simplifies to

$$(p_1 - p_2)_{y=y_I} = P_1 - P_2 - \int_{x_0}^x (\chi_1 - \chi_2) d\eta + \rho_1 (1 - \delta) g_y y_I = -\gamma \frac{\partial^2 y_I}{\partial x^2}, \quad (3.6)$$

where the curvature has been approximated with the negative of the second derivative of the interface elevation on the right-hand side. Differentiating (3.6) with respect to  $x$  and rearranging, we obtain

$$\chi_2 = \chi_1 - \rho_1 (1 - \delta) g_y y_I' - \gamma' y_I'' - \gamma y_I''', \quad (3.7)$$

where a prime denotes a partial derivative with respect to  $x$ . Using (3.7) to eliminate  $\chi_2$  in favour of  $\chi_1$  from (3.5), we find

$$u_I = \frac{2h^2}{\mu_1} \frac{r}{(1+r)^2(\lambda+r)} \left[ (1+r)\chi_1 - \rho_1 (1 - \delta) g_y r y_I' - r \gamma' y_I'' - r \gamma y_I''' + \rho_1 g_x (1 + \delta r) \right] + \frac{rU_1 + \lambda U_2}{\lambda + r} + \frac{h_2}{\mu_1(\lambda + r)} \gamma'. \quad (3.8)$$

To derive an evolution equation for the interface, we first integrate both sides of (3.1) with respect to  $y$  over the respective domains of definition and substitute for the shear stresses using (3.2) to find the following expressions for the flow rates in terms of the interfacial velocity:

$$Q_j = \frac{\chi_j + \rho_j g_x}{12\mu_j} h_j^3 + \frac{1}{2} (u_I + U_j) h_j. \quad (3.9)$$

Now, a mass balance over the channel cross-section requires

$$\frac{\partial h_j}{\partial t} = -\frac{\partial Q_j}{\partial x}, \quad (3.10)$$

for  $j = 1, 2$ . Since  $h_1 + h_2 = 2h$  is constant, the total flow rate  $Q = Q_1 + Q_2$  must be independent of  $x$ , and thus

$$Q(t) = \frac{\chi_1 + \rho_1 g_x}{12\mu_1} h_1^3 + \frac{1}{2}(u_l + U_1)h_1 + \frac{\chi_2 + \rho_2 g_x}{12\mu_2} h_2^3 + \frac{1}{2}(u_l + U_2)h_2. \quad (3.11)$$

Substituting the right-hand side of (3.8) for the interfacial velocity and rearranging, we obtain

$$\begin{aligned} -\chi_1 \equiv \frac{\partial p^{(1)}}{\partial x} = \frac{\mu_1}{D} \left\{ -\frac{\rho_1(1-\delta)g_y}{\mu_1} \left( h_2 + 6\frac{\lambda}{\lambda+r}h \right) h_2^2 y_l' - \frac{\gamma}{\mu_1} \left( h_2 + 6\frac{\lambda}{\lambda+r}h \right) h_2^2 y_l'' \right. \\ \left. + \frac{\rho_1 g_x}{\mu_1} \left( \lambda h_1^3 + \delta h_2^3 + 6(1+\delta r)\frac{\lambda}{\lambda+r} h h_1 h_2 \right) + 12\lambda h \left( \frac{U_1 + rU_2}{1+r} + \frac{rU_1 + \lambda U_2}{\lambda+r} \right) \right. \\ \left. + \frac{12}{\mu_1} \frac{\lambda}{\lambda+r} h h_2 \gamma' - \frac{1}{\mu_1} \left( 6h\frac{\lambda}{\lambda+r} + h_2 \right) h_2^2 \gamma' y_l'' - 12\lambda Q(t) \right\}, \end{aligned} \quad (3.12)$$

where

$$D = \lambda h_1^3 + h_2^3 + 12\frac{\lambda}{\lambda+r} h^2 h_2. \quad (3.13)$$

If the flow is periodic with period  $L$ , the flow rate  $Q(t)$  is evaluated by specifying the pressure drop over one period,

$$\Delta p^{(1)}(t) = \Delta p^{(2)}(t) = p^{(i)}(x+L, y, t) - p^{(i)}(x, y, t), \quad (3.14)$$

where  $i = 1$  or  $2$ . In the case of pure shear- or gravity-driven flow,  $\Delta p^{(1)}(t) = 0$ .

An evolution equation for the interfacial position,  $y_l(x, t)$ , arises by substituting the expression for  $\chi_1$  given in (3.12) into (3.8) and (3.9) written for  $j = 1$ , and the resulting expression for the flow rate into (3.10) written for  $j = 1$ . The result is

$$\frac{\partial y_l}{\partial t} = F(y_l, y_l', y_l'', y_l''', y_l^{iv}), \quad (3.15)$$

where the function  $F$  has a strongly nonlinear dependence on its arguments. Under the premise of the lubrication approximation, the surfactant transport equation (2.3) with  $w = 0$  simplifies to the Eulerian one-dimensional convection–diffusion equation

$$\frac{\partial \Gamma}{\partial t} + \frac{\partial(u_l \Gamma)}{\partial x} = D_s \frac{\partial^2 \Gamma}{\partial x^2}. \quad (3.16)$$

The evolution of long waves is governed by the system of equations (3.15) and (3.16), subject to an initial condition for the interface position and surfactant concentration.

In the context of the lubrication approximation, surface tension is important only when the capillary pressure is comparable to, or larger than, the viscous shear stress due to the perturbation. In the case of a periodic flow with period  $L$ , we scale the former with  $\gamma_0 \epsilon h/L^2$  and the latter with  $\mu_1 \epsilon \xi_1$ , where the dimensionless number  $\epsilon$  expresses the magnitude of the perturbation, and derive the condition  $Ca \lesssim (h/L)^2$ . When this condition is not met, the surface tension contributes a harmless higher-order term that is inconsequential to the leading-order dynamics. Similarly, assuming that  $Ma$  is of order unity, the Marangoni stress will be important only when  $Ca \lesssim h/L$ .

### 3.2. Linear evolution of long waves

To examine the evolution of waves whose amplitude is small compared to the wavelength  $L$ , we carry out a linear stability analysis based on the evolution equations derived previously in this section. Appealing to a generalized version of Squire's

theorem (Hesla, Pranckh & Preziosi 1986; Halpern & Frenkel 2003), we restrict our attention to two-dimensional disturbances in the  $(x, y)$ -plane, introduce a small parameter  $\varepsilon$ , and consider the normal-mode expansions

$$y_I(x, t) = y_0 + \varepsilon A_1 e^{ik(x-ct)} + \text{c.c.}, \quad \Gamma(x, t) = \Gamma_0 + \varepsilon \Gamma_1 e^{ik(x-ct)-i\phi} + \text{c.c.},$$

where  $k = 2\pi/L$  is the wavenumber,  $c = c_r + ic_i$  is the complex phase velocity,  $A_1$  and  $\Gamma_1$  are disturbance amplitudes, and *c.c.* denotes a complex conjugate. The constant  $\phi$  expresses the phase lag between the interface and surfactant concentration wave. Substituting the normal-mode expansions into (3.15) and (3.16) and linearizing in the usual way, we derive a pair of evolution equations for the interface position and surfactant concentration perturbation amplitudes  $A_1$  and  $\Gamma_1$ , which may be written in the matrix form  $\mathbf{B} \cdot \mathbf{x} = \mathbf{0}$ , where  $\mathbf{x} = (A_1, \Gamma_1)^T$ . To ensure a non-trivial solution, we require  $\text{Det}(\mathbf{B}) = 0$ , and obtain a quadratic equation for the complex phase velocity,  $c$ , revealing the existence of two normal modes. In practice, to cope with the large amount of algebra, we perform the linearization using the computer algebraic manipulation package Maple, and run the code for individual cases with specific parameter values.

An alternative formulation of the linear stability problem relies on the Orr–Sommerfeld equation for the disturbance stream function, applied in the limit of Stokes flow (Frenkel & Halpern 2002). The procedure involves introducing expansions with respect to the reduced wavenumber  $kh$  to generate a sequence of eigenvalue problems. Satisfaction of the boundary conditions yields a quadratic equation for  $c$ .

The dimensionless growth rate of interfacial waves,  $s = (\mu_1/\gamma_0)kh c_I$ , depends on the dimensionless groups identified at the end of §2, where  $c_I = \text{Im}(c)$ , and  $k = 2\pi/L$  is the wavenumber. It is worth emphasizing that the structure of the base flow influences the growth rate only insofar as it determines the interfacial shear rates  $\xi_1$  and  $\xi_2$ , and this is consistent with physical intuition, which suggests that small enough deflections of the interface from the initial position only feel the shearing effect of the local undisturbed velocity profile in the surfactant transport equation. In the absence of surfactants or when  $Ma = 0$ , the surviving normal mode is stable, and the rate of decay is independent of  $Ca$ . The non-dimensional phase velocity  $v_p = (\mu_1/\gamma_0)kh c_R$ , where  $c_R = \text{Re}(c)$ , also depends on the undisturbed interfacial velocity, but if a change is made to a frame of reference moving with the speed of the unperturbed interface, the extra dependence disappears. To isolate the Marangoni instability, henceforth we consider fluids with equal density,  $\delta = 1$ , thereby eliminating the possibly destabilizing influence of gravity. In addition, because the diffusivity of most common surfactants is small, we shall present results for  $D_s = 0$  corresponding to the limit of infinite Péclet number.

Figure 2(a,b) shows graphs of the dimensionless growth rate of the stable and unstable normal mode, for a series of capillary numbers and a fixed Marangoni number, generated using the Maple code. Note that, as  $kh \rightarrow 0$ , the leading-order predictions for the growth rates tend to become independent of the capillary number. The results confirm the findings of Frenkel & Halpern (2002), showing that introducing a surfactant produces instability over a range of wavenumbers subtended from zero to a critical value corresponding to neutral stability. In particular, as the capillary number approaches zero, the range of unstable wavenumbers shrinks gradually, and the growth rates tend smoothly to finite values; thus, the limit  $Ca \rightarrow 0$  is regular. This non-singular behaviour appears at first to be at odds with the findings of Frenkel & Halpern (2002), who identified an apparent discontinuity at  $Ca = 0$ . In later work, Halpern & Frenkel (2003) resolved the issue by noting a non-uniformity

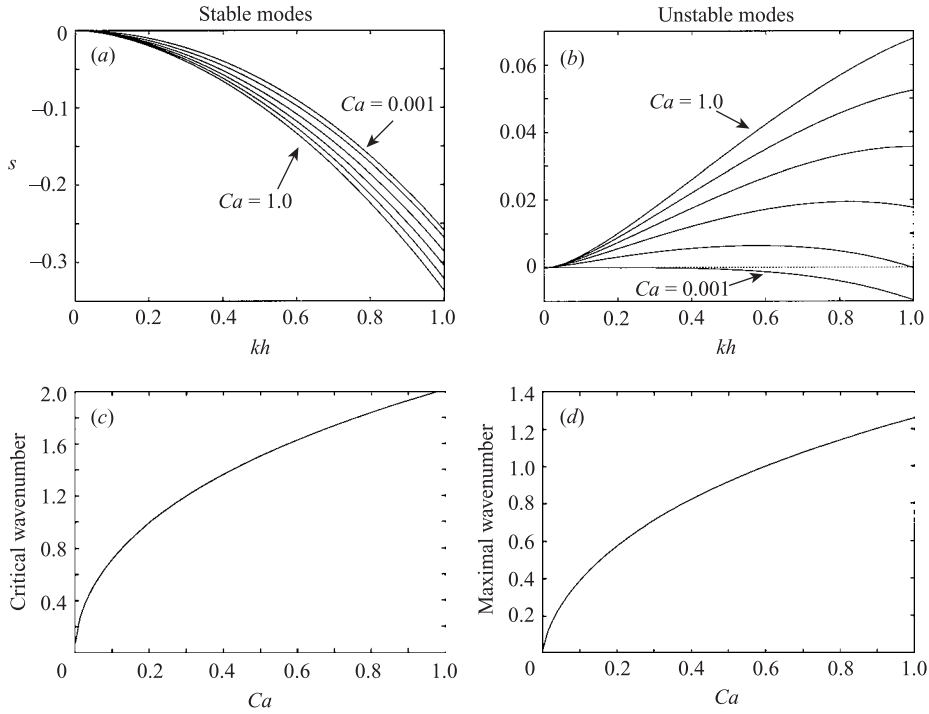


FIGURE 2. Stability of two-layer flow for layer thickness ratio  $h_1/h_2=1/3$ ,  $\lambda=0.5$ ,  $Ma=1$ , and  $\theta_0=0$ . Graphs of the dimensionless growth rate  $s$  against the wavenumber for (a) the stable, and (b) the unstable normal mode. The capillary numbers are evenly spaced over the range  $10^{-3} \leq Ca \leq 1$ . (c) Critical wavenumber  $kh$  for neutral stability, and (d) wavenumber corresponding to the maximum growth rate of the unstable mode.

in the small-wavenumber expansion in the limit of vanishing capillary number. In fact, the particular form of the expansion is modified as  $Ca \rightarrow 0$ , allowing the growth rate to proceed smoothly through the limit.

Figure 2(c,d) displays the critical wavenumber  $kh$  beneath which the flow is unstable, and the wavenumber corresponding to the maximum growth rate of the unstable normal mode for the given set of parameters. These graphs illustrate that instability occurs as soon as the capillary number becomes non-zero, that is the flow is unstable as long as the shear rate of the unperturbed flow at the interface does not vanish. The higher the capillary number, the larger the wavenumber of the most unstable mode. When the unperturbed interface lies in the middle of the channel,  $y_0=0$  and  $h_1=h_2$ , it can be shown that the complex wave speed for both modes lies in the lower half of the complex plane under all conditions, and so the flow is stable. Unfortunately, a compelling physical reason for this behaviour could not be identified. In contrast, Yih (1967) showed that two-fluid plane Poiseuille flow is unstable at any non-zero Reynolds number when the unperturbed interface lies midway between the channel walls.

To illustrate the effect of the layer thicknesses, in figure 3 we display graphs of the reduced growth rate,  $s_1 = (\mu_1/\gamma_0)kh_1 c_I$ , plotted against the unperturbed layer thickness ratio, for reduced wavenumbers  $kh_1 = 0.1, 0.05$ , and  $0.01$ . Note that the growth rate has been non-dimensionalized with respect to the fixed thickness of the lower layer; accordingly a new capillary number has been introduced,  $Ca_1 = \xi_1 h_1 \mu_1/\gamma_0$ .

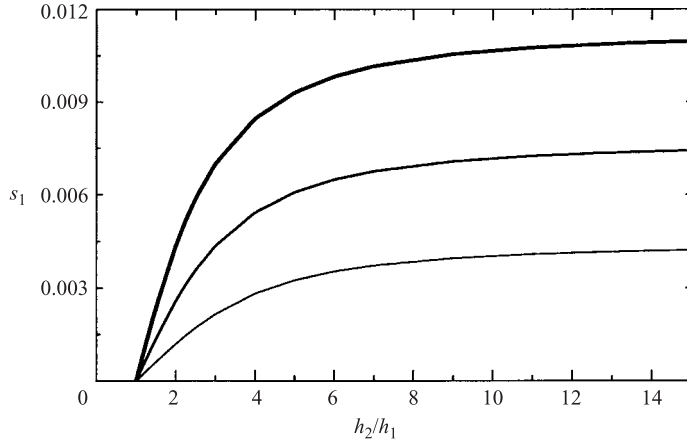


FIGURE 3. Dominant dimensionless growth rate,  $s_1 = \mu_1 kh_1 c_1 / \gamma_0$ , for a channel of varying width,  $\theta_0 = 0$ ,  $\lambda = 0.5$ ,  $Ca_1 = 1.0$ , and  $Ma = 1.0$ , and reduced wavenumbers  $kh_1 = 0.1$  (thick line),  $kh_1 = 0.075$  (intermediate line), and  $kh_1 = 0.05$  (thin line.)

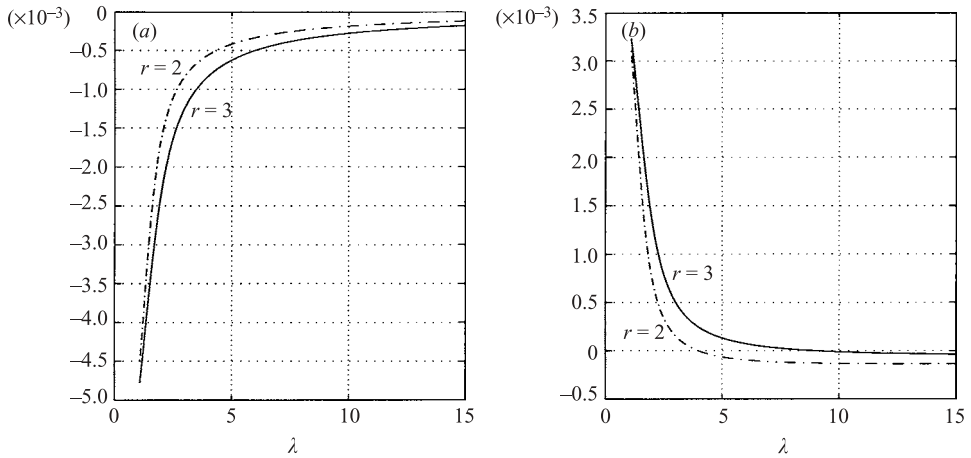


FIGURE 4. Effect of the viscosity ratio  $\lambda$  on the reduced growth rate  $s$  for  $Ca = 1$ ,  $Ma = 1$ ,  $kh = 0.1$ , and  $r = h_2/h_1 = 2$  and 3; (a) recessive mode, and (b) dominant mode.

For the conditions stated in the figure caption, the presence of the upper wall has a small effect on the growth rate beyond  $h_2/h_1 \simeq 15$ . For  $h_2/h_1 = 1$ , corresponding to the limit  $y_0 \rightarrow 0$ , the curve appears to predict a zero growth rate and thus a neutrally stable flow, which seemingly contradicts our earlier remark concerning the case  $y_0 = 0$ . In fact, the growth rate is only fractionally less than zero and thus small perturbations do decay, but very slowly.

Since channel-flow instability in the absence of surfactants is associated with viscosity variation or stratification, it is of particular interest to examine the significance of the viscosity ratio  $\lambda$ . In figure 4, we plot the growth rates of the two normal modes for flow in a horizontal channel, with  $kh = 0.1$ ,  $Ca = 1$ ,  $Ma = 1$ , and two values of the unperturbed layer thickness ratio,  $r \equiv h_2/h_1 = 2$  (broken line) and 3 (solid line). The first growth rate, plotted in figure 4(a), is apparently negative for all values of  $\lambda$ , while the second growth rate, plotted in figure 4(b), is positive for small values of  $\lambda$ , passes through zero at  $\lambda \approx r^2$ , and remains negative thereafter.

$L/h:$	$2\pi$		$4\pi$		$8\pi$	
$s$	-0.5357	0.0250	-0.1449	0.0250	-0.0418	0.0123
$\text{Arg}(\tau)/\pi$	0.0720	1.4046	0.0903	1.4068	0.0997	1.4000
$ \tau $	3.9368	1.7315	4.6002	2.9557	5.4339	5.0043

TABLE 1. Properties of the lubrication-flow stable (left-hand columns) and unstable (right-hand columns) normal modes for  $h_1/h_2 = 1/2$ ,  $\lambda = 0.5$ ,  $Ca = 0.6$ ,  $Ma = 2$  and  $\theta_0 = 0$ .

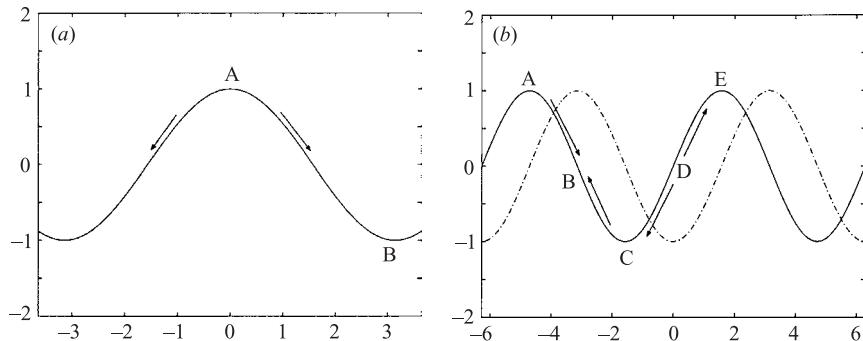


FIGURE 5. Sketch of the Marangoni flows (shown as arrows), for (a) the stable mode, and (b) the unstable mode. The interfacial wave is shown as a solid line, and the surfactant wave perturbation is shown as a broken line.

Thus, increasing the viscosity contrast beyond a threshold suppresses the Marangoni instability (see also Frenkel & Halpern 2002; Halpern & Frenkel 2003).

### 3.3. Structure of the normal modes

It is illuminating to examine in some detail the structure of the normal modes. Table 1 displays the growth rate, phase shift, and reduced amplitude of the surfactant concentration wave relative to the interfacial wave for the conditions displayed in the caption. For convenience, we have introduced the dimensionless complex group  $\tau \equiv \Gamma_1 h / \Gamma_0 A_1$  expressing the relative amplitude and phase shift of the surfactant concentration relative to the interfacial wave. The properties of the normal modes for other parameter values are close to those displayed in the table. The results show that the relative amplitude of the surfactant concentration wave for the unstable normal mode is consistently lower than that for the stable normal mode. More important, the phase shift expressed by  $\text{Arg}(\tau)$  is close to 0.1 for the stable mode, and close to  $1.4\pi$  for the unstable mode.

The significance of these results becomes evident on observing that, when the phase lag is equal to 0 or  $2\pi$ , the Marangoni stresses suppress the instability, as illustrated in figure 5(a). Physically, the surfactant level is high and correspondingly the surface tension is low at the crest (point A), as required by equation (2.1), while the converse is true at point B. A local flow is thus induced from A to B in order to generate the shear stress required to balance the Marangoni traction. In contrast, when the phase lag is equal to  $\pi$ , Marangoni stresses drive a flow from the troughs to the crests of the interfacial wave, thereby promoting the instability.

A sketch of the relative wave configuration at the mid-points  $kx = \pi/2$  or  $3\pi/2$ , is shown in figure 5(b). The surface tension is higher at A and C than at B, and lower at C and E than at D. Thus, Marangoni flows are induced in the directions of the arrows

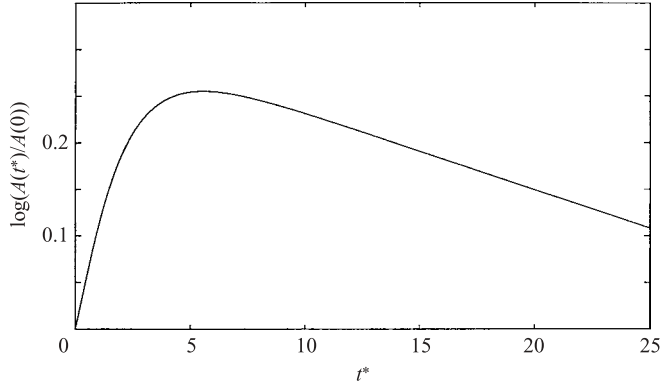


FIGURE 6. Evolution of the interface amplitude for an arbitrary sinusoidal perturbation showing transitory growth prior to long-term decay, for  $h_1/h_2 = 2/3$ ,  $\lambda = 0.5$ ,  $Ca = 0.1$ ,  $Ma = 2.0$ ,  $\theta_0 = 0$ , and  $kh = 1.0$ .

shown, and the tendency now is for some fluid to be drawn away from D toward C and E, while fluid is also carried toward B from A and C. This qualitative reasoning suggests that a phase lag in the range  $(\pi/2, 3\pi/2)$  is necessary for instability. It is interesting that the actual phase lag for the unstable modes is a slight shift from  $3\pi/2$  into the unstable range. Overall, the present interpretation in terms of the phase shift is consistent with the discussion of Frenkel & Halpern (2002) and Halpern & Frenkel (2003).

#### 3.4. Numerical simulations

For a given initial condition, the coupled evolution equations (3.15) and (3.16) were integrated in time using the second-order Runge–Kutta method. Centred differences were applied for the computation of the spatial derivatives involved in both equations, and the time step was set at a sufficiently small value to stabilize the numerics. Typically, 64 evenly spaced grid points were used with a dimensionless time step  $\xi_1 \Delta t$  on the order of  $10^{-3}$ . An independent scheme for solving the surfactant transport equation was implemented to monitor the effect of numerical diffusion and provide a check on accuracy (Ni 1982). This scheme essentially splits the discretized forms of the derivatives occurring in (3.16) into sums of forward and backward differences, resulting in a method that is second-order accurate in both time and space.

An arbitrary sinusoidal initial profile for the interface position and surfactant concentration generally contains a combination of the two normal modes. As the integration continues in time, eventually only the dominant unstable mode survives. However, even with a set of purely decaying modes, the solution to a dynamical system may exhibit significant transitory growth prior to the long-term decay, provided that the differential operator of the linearized system exhibits non-orthogonal eigenmodes (Trefethen *et al.* 1993). A sample calculation displayed in figure 6 demonstrates this occurrence in our two-layer fluid problem for an arbitrary initial perturbation defined by  $|\tau| = 2.95571$  and  $\text{Arg}(\tau) = 1.4068\pi$ . In this example, linear theory predicts a pair of stable normal modes with non-dimensional growth rates  $s = -0.5052$  and  $-8.532 \times 10^{-3}$ . In the figure,  $\log(A(t^*)/A(0))$  is plotted against the non-dimensional time  $t^* = \gamma_0 t / h\mu_1$ , where  $A$  is the amplitude of the interfacial wave. During the early stages of the evolution, the wave undergoes a period of growth before ultimately decaying at a rate  $-8.2 \times 10^{-3}$ , which is close to that of the least stable mode.

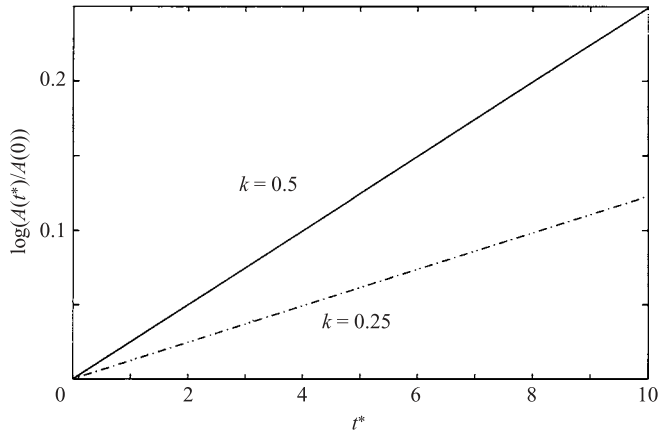


FIGURE 7. Evolution of the interfacial amplitude subject to a normal-mode perturbation for  $h_1/h_2 = 1/2$ ,  $\lambda = 0.5$ ,  $Ca = 0.6$ ,  $Ma = 2$ , and  $\theta_0 = 0$ . The initial data correspond to the growing mode predicted by linear stability theory; (i)  $kh = 0.5$ ,  $|\tau| = 2.9557$ ,  $\text{Arg}(\tau) = 1.4068\pi$ , and (ii)  $kh = 0.25$ ,  $|\tau| = 5.0043$ ,  $\text{Arg}(\tau) = 1.4000\pi$ .

By a judicious choice of initial conditions, we may isolate the dominant mode at the outset. This is achieved by using the predictions of the linear theory to furnish starting profiles for the interfacial and surfactant concentration waves with a specific amplitude ratio and phase shift. Results for  $h_1/h_2 = 1/2$ ,  $Ca = 0.6$ ,  $Ma = 2$ , and wavenumbers  $kh = 0.5$  and  $0.25$  are shown in figure 7, where it is clear that the growing normal modes are picked up straightaway. Numerically fitting the slopes of the two lines, we obtain the estimates  $s = 0.0249$  for  $kh = 0.5$ , and  $s = 0.0123$  for  $kh = 0.25$ , which agree with the predictions of the linear theory to the shown accuracy.

It is of interest to describe the shape of the interface after the perturbation has grown to a finite amplitude and the evolution has exceeded the bounds imposed by linear theory. In particular, it is of interest to examine whether the instability saturates due to nonlinear interactions and the wave attains a fixed amplitude. Figure 8 confirms this possibility by presenting an example where the nonlinear evolution of an arbitrary (non-normal mode) initial perturbation leads to saturation. In figure 8(b), the saturated interfacial and surfactant waves are both displayed together with their initial profiles. Wave steepening and the formation of saw-tooth profiles are important features of the motion. Similar saturation is observed for other cases considered.

#### 4. Linear stability of Stokes flow

Halpern & Frenkel (2003) performed a linear stability analysis of the two-layer flow for arbitrary wavenumbers, in the limit of Stokes flow. To establish a point of reference for the lubrication-flow analysis discussed in §3, we have repeated the linear analysis, also including the effects of gravity and surfactant surface diffusivity. The essential details are outlined in Appendix A. The end product is a quadratic equation for the complex wave speed, corresponding to two normal modes. In some special cases, including the case of equal layer thicknesses, the roots can be found in analytical form. More generally, we use the computer algebra package Maple to obtain the coefficients of the quadratic equation for the complex phase velocity  $c$ , and hence the growth rates in terms of expressions that are too lengthy to reproduce. In practice, appropriate parameter values are inserted into these exact expressions to

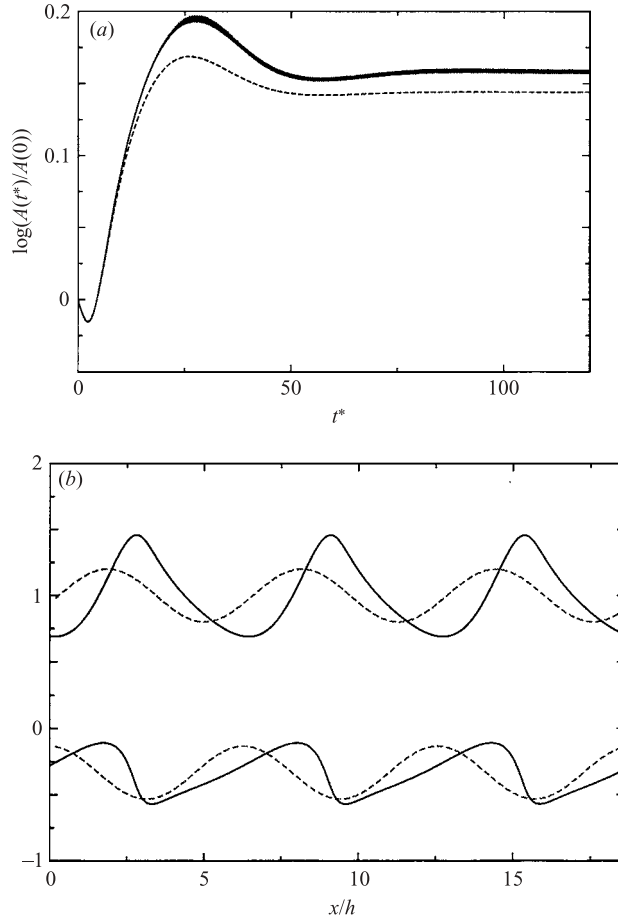


FIGURE 8. Finite-amplitude evolution of a long wave with initial amplitude  $|A_1|/h=0.2$ , for  $h_1/h_2=1/2$ ,  $\lambda=0.5$ ,  $Ca=0.6$ ,  $Ma=2$ ,  $\theta_0=0$ , and  $L/h=2\pi$ . (a) Graph of  $\log(A(t^*)/A(0))$  for  $N=64$  (solid line) and 128 (broken) finite-difference divisions. (b) Saturated instability waves (solid lines) arising from the initial profiles drawn with broken lines. The upper and lower sets depict, respectively, the surfactant and interfacial waves.

obtain numerical values. When the unperturbed layer thicknesses are equal, the two normal modes are found to be stable under any conditions.

In the absence of a surfactant or when  $Ma=0$ , the coefficient of the quadratic term becomes zero, leaving a linear equation corresponding to a single normal mode. In that case, the imaginary part of  $c$  turns out to be independent of the interfacial shear rate, that is, the growth rate is independent of the structure of the base flow and equal to that of the interface between two superposed stationary layers in a channel confined between two parallel plane walls. Expressions for the rate of decay in the limit where one or both of the layer thicknesses are large compared to the channel semi-width can be derived in analytical form (e.g. Pozrikidis 2004).

The range of validity of the lubrication approximation can be estimated by comparing the long-wave linear growth rates deduced from the analysis of §3.1 with the exact growth rates deduced from the linear analysis of the Stokes flow problem. Figure 9(a) shows results for a typical case over a range of wavenumbers, in the absence of surfactants. In view of the conditionally small wavenumber, the strong

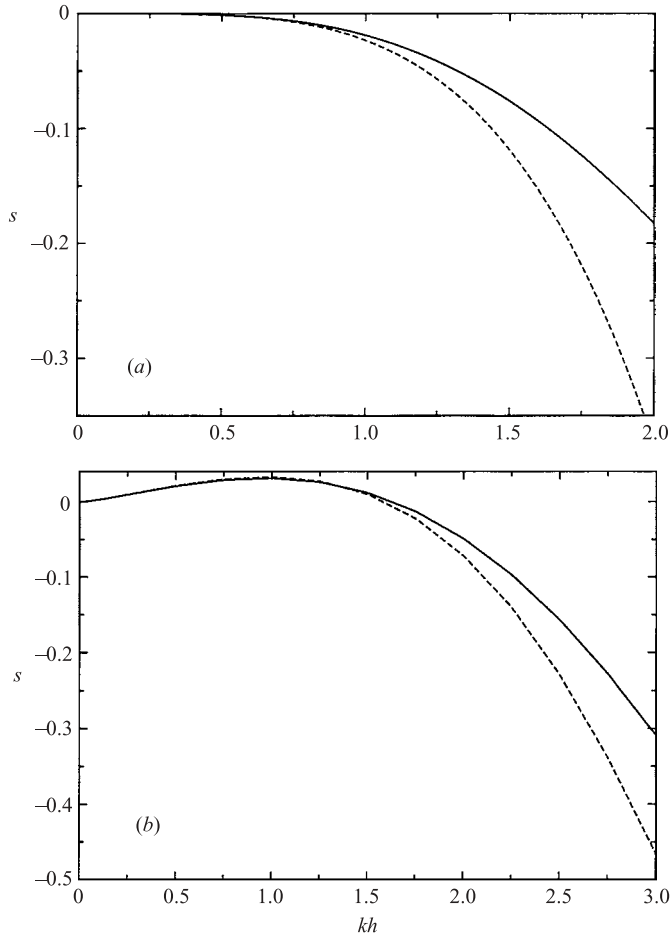


FIGURE 9. (a) Comparison of growth rates for Stokes flow (solid lines) and lubrication flow (broken lines) for  $h_1/h_2 = 1/3$ ,  $\lambda = 0.5$ ,  $Ca = 0.57$ , and  $\theta_0 = 0$ , in the absence of surfactants,  $Ma = 0$ . (b) The dominant mode for a contaminated interface with  $Ma = 1$ .

performance of the lubrication analysis up to quite sizeable wavenumbers is striking. In this case, the lubrication approximation yields predictions accurate to within 5% relative error for reduced wavenumbers less than 0.45.

Figure 9(b) compares the two predictions in the presence of surfactants. Once again, we observe good agreement between the two theories up to moderate wavenumbers. In fact, the range of validity of the long-wave predictions appears to have been extended. Now, the long-wave results are accurate to within 5% for reduced wavenumbers up to 0.88, and to within 1% for reduced wavenumbers up to 0.32. Taking instead  $Ca = 1.14$  with all other parameters held fixed, we find that the long-wave results are accurate to within 1% for reduced wavenumbers up to 0.31. Consequently, the range of validity would appear to be insensitive to the capillary number. If we raise the Marangoni number to 2.0 instead, we find that the long-wave results are accurate to within 1% for reduced wavenumbers up to 0.36, and so the range of validity is slightly increased. Raising the viscosity contrast does not have a significant effect. For example, the results shown in figure 4 for  $kh = 0.1$  are accurate to within 0.1% when  $\lambda = 12$ .

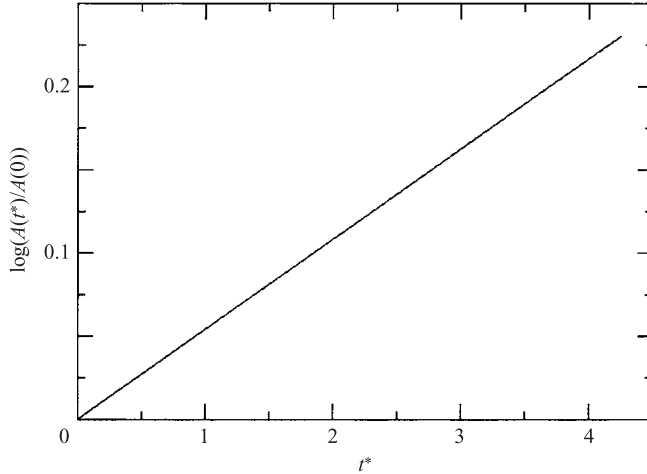


FIGURE 10. Growth curve for  $h_1/h_2 = 1/3$ ,  $\lambda = 0.5$ ,  $Ca = 1.0$ ,  $Ma = 0.5$ ,  $\theta_0 = 0$ , and  $kh = 1$ , showing the onset of the Marangoni instability subject to a normal-mode perturbation.

## 5. Numerical study of Stokes flow

In the last part of this investigation, we relax the restrictions on wavelength and amplitude imposed by the lubrication approximation and linear theory, and consider the evolution of interfacial waves in the context of Stokes flow. In the limit of vanishing Reynolds number, the motion of each fluid is governed by the linear equations of Stokes flow,

$$\mathbf{0} = -\nabla p^{(j)} + \mu_j \nabla^2 \mathbf{u}^{(j)} + \rho_j \mathbf{g}, \quad \nabla \cdot \mathbf{u}^{(j)} = 0, \quad (5.1)$$

for  $j = 1, 2$ . At the interface, the surface traction suffers a discontinuity due to the surface tension, given by

$$\Delta \mathbf{f} \equiv (\boldsymbol{\sigma}^{(1)} - \boldsymbol{\sigma}^{(2)}) \cdot \mathbf{n} = \gamma \kappa \mathbf{n} - \frac{\partial \gamma}{\partial l} \mathbf{t}, \quad (5.2)$$

where  $\boldsymbol{\sigma}^{(j)}$  is the stress tensor in each of the two fluids, and the unit normal vector  $\mathbf{n}$  points into the lower fluid 1, as shown in figure 1. Numerical solutions for arbitrary amplitudes were computed based on a generalization of the boundary-integral formulation for two-layer periodic channel flow developed by Pozrikidis (1992, 1997a, 2003). For clarity, the essential details of this formulation are outlined in Appendix B along with an overview of the numerical method.

The linear stability analysis of §4 (see Appendix A) reveals that, in the absence of surfactants, the flow is always stable. However, instability does arise for a contaminated interface, as illustrated in figure 10 for the conditions described in the caption. This simulation was initiated with interfacial and surfactant concentration waves whose complex amplitudes correspond to the dominant normal mode deduced from the Stokes-flow linear analysis, described by  $|\tau| = 7.8915$  and  $\text{Arg}(\tau) = 1.3576 \pi$ . The straight line obtained with an approximate slope of 0.06 is in good agreement with linear theory, predicting a slope of 0.0555.

Figure 11(a) shows the effect of the Marangoni number on the growth rate, computed using the results of the linear analysis, revealing the occurrence of a peak at  $Ma \approx 1.2$ . Figure 11(b) illustrates the variation of the peak value with the wavenumber. Increasing the viscosity ratio while holding all other parameters fixed

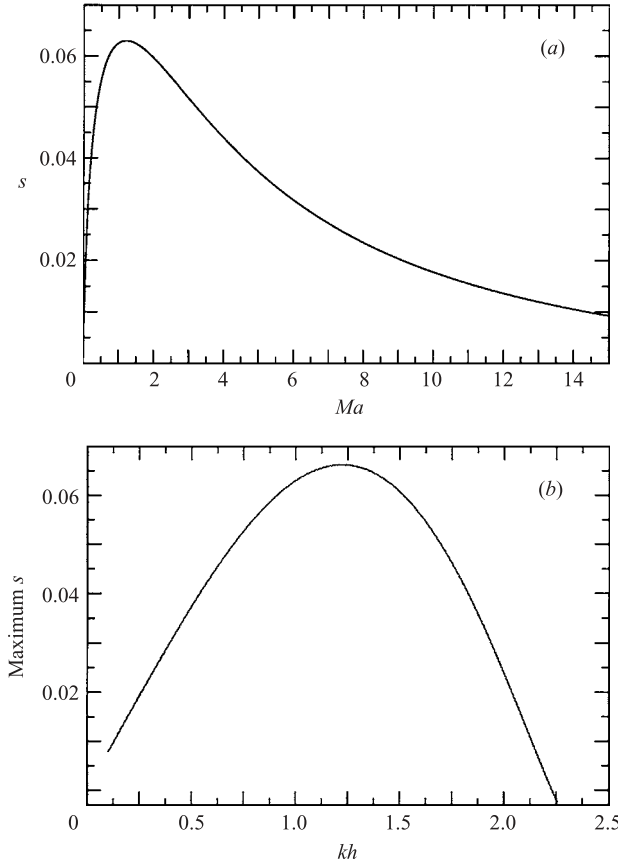


FIGURE 11. Instability in Stokes flow for  $h_1/h_2=1/3$ ,  $\lambda=0.5$ ,  $Ca=1.0$ , and  $\theta_0=0$ ; (a) dominant growth rate over a range of Marangoni numbers for  $kh=1$ , (b) dependence of the maximum growth rate on the wavenumber.

reduces the dominant growth rate until finally it attains a negative value and the flow is stabilized.

Estimates for the growth rates of both normal modes can be obtained from numerical simulations of the small-amplitude motion beginning with an arbitrary set of initial conditions, and applying Prony's method of complex exponential fitting (e.g. Hildebrand 1974, pp. 457–463; Kay & Marple 1981; Marple 1987, pp. 303–349). This technique has been applied successfully by Pozrikidis (1998*b*) to the problem of multi-layered film flow down an inclined plane. To implement the method, we express the disturbance in the interface position or surfactant concentration as a combination of evolving cosine and sine waves, writing, for example,

$$\Gamma(x, t) = \Gamma_0 + F_c(t) \cos kx + F_s(t) \sin kx. \quad (5.3)$$

The coefficients  $F_c(t)$  and  $F_s(t)$  are computed by numerical integration from the actual profiles obtained by the boundary-element simulation. The aim is to construct best-fit estimates for the coefficients in the complex exponential forms

$$F_c(t) = \frac{1}{2} \sum_{l=1}^N \{c_c^{(l)} \exp(-i\sigma_l t) + \text{c.c.}\}, \quad F_s(t) = \frac{1}{2} \sum_{l=1}^N \{c_s^{(l)} \exp(-i\sigma_l t) + \text{c.c.}\}, \quad (5.4)$$

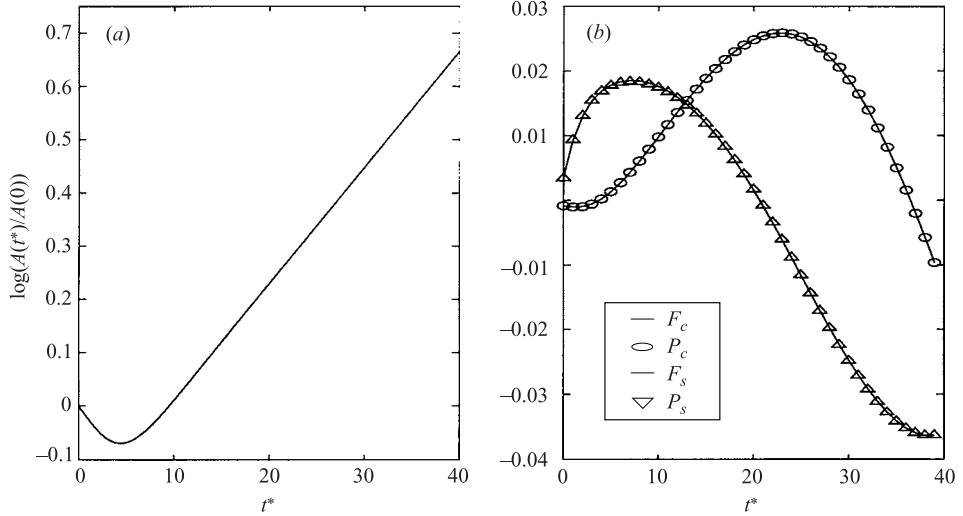


FIGURE 12. Stokes flow simulation for  $Ca=0.6$ ,  $Ma=2$ ,  $\lambda=0.5$ ,  $\theta_0=0$ ,  $h_1/h_2=1/2$ , and  $L/h=2\pi$ . (a) Evolution of the reduced amplitude  $\log(A(t^*)/A(0))$ , and (b) time-series coefficients  $F_c(t)$ ,  $F_s(t)$  in comparison with their estimated two-mode Prony fits  $P_c(t)$  and  $P_s(t)$  shown with the symbols.

where  $N$  is the number of normal modes, and c.c. denotes a complex conjugate. The complex coefficients  $c_s^{(l)}$ ,  $c_c^{(l)}$  and growth rates  $\sigma_l$  are computed as part of the Prony fitting process.

Figure 12 displays the wave amplitude evolution along with results of two-mode exponential fitting,  $N=2$ , for  $\lambda=0.5$ ,  $Ca=0.6$ ,  $Ma=2$ , and  $L/h=2\pi$ . The Prony estimate of the dominant growth rate,  $s=0.023$ , compares well with the value 0.022 found both by estimating the slope of the curve shown in figure 12(a) and from the linear stability analysis. For the recessive mode, the Prony fitting gives  $s=-0.41$ , which is in fair agreement with a theoretical value of  $-0.44$ . However, while the Prony estimates of the growth rates are encouraging, corresponding estimates of the crest speed are poor, as is the prediction of the initial wave amplitude. This weakness was traced to the disparate magnitude of the growth rates of the normal modes. Overall, we find that the Prony fitting method is a helpful but not definitive means of extracting the complete properties of these slowly growing normal modes.

Next, we consider differences in behaviour predicted by the long-wave approximation and the Stokes flow simulations for small and moderate wavenumbers. Figure 13 compares the two predictions for  $h_1/h_2=1/2$ ,  $\lambda=0.5$ ,  $Ca=0.6$  and  $Ma=2$ , for the three wavelengths  $L/h=2\pi$ ,  $4\pi$ ,  $8\pi$ , starting with an arbitrary (non-normal mode) initial condition. The non-dimensional growth rates obtained by estimating the slopes of the curves for  $L/h=\pi$ ,  $2\pi$ ,  $4\pi$ , and  $8\pi$ , are  $s=-0.173$ , 0.022, 0.024, and 0.011 in the case of Stokes flow, and  $s=-0.241$ , 0.025, 0.025, and 0.011 in the case of the lubrication approximation. These values are comparable with those quoted in tables 1 and 2, obtained from the linear stability analysis.

Evidently, the agreement between the long-wave and Stokes-flow calculations improves as the wavelength increases. More important, the lubrication approximation furnishes accurate predictions of the most unstable wavenumber, thereby providing support for the physical relevance of the results discussed in §3. A Stokes flow simulation for wavelengths  $L/h=4\pi$  and  $8\pi$  subject to an initial condition

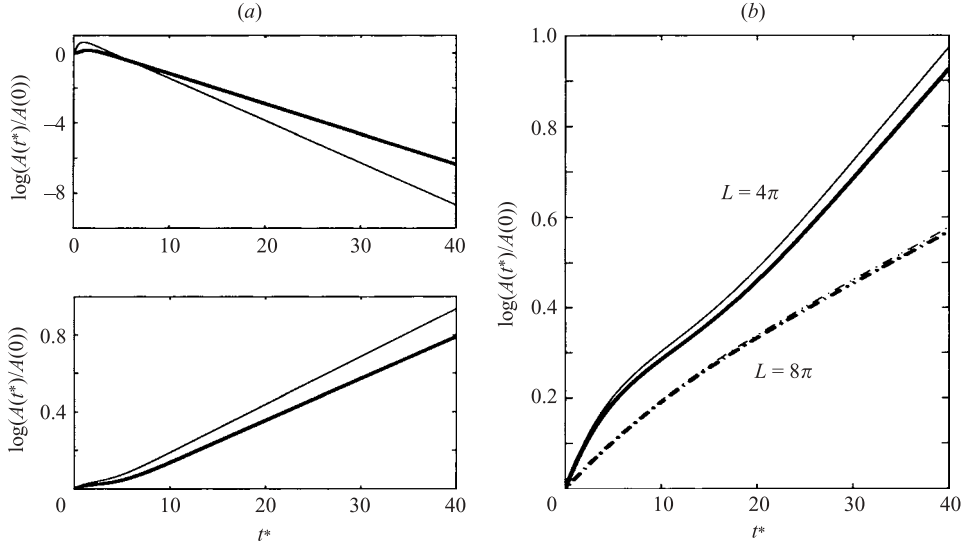


FIGURE 13. Comparison of the long-wave analysis (thin lines) and Stokes flow results (thick lines) for  $h_1/h_2 = 1/2$ ,  $\lambda = 0.5$ ,  $Ca = 0.6$ ,  $Ma = 2$ , and  $\theta_0 = 0$ : (a) (upper)  $L/h = \pi$ , and (lower);  $2\pi$ : (b)  $L/h = 4\pi$  and  $8\pi$ .

---

$L/h$ :	$2\pi$		$4\pi$		$8\pi$	
$s$	-0.4415	0.0218	-0.1380	0.0241	-0.0413	0.0122
$\text{Arg}(\tau)/\pi$	0.0776	1.4048	0.0923	1.4050	0.1003	1.3993
$ \tau $	4.5872	1.974	4.7892	3.0496	5.4932	5.0397

---

TABLE 2. Properties of the Stokes-flow stable (left-hand columns) and unstable (right-hand columns) modes, for  $h_1/h_2 = 1/2$ ,  $\lambda = 0.5$ ,  $Ca = 0.6$ ,  $Ma = 2$ , and  $\theta_0 = 0$ .

corresponding to the dominant normal modes extracted from the long-wave analysis produces two straight lines on a  $\log(A(t^*)/A(0))$  versus time plot, similar to those seen in figure 7, with slopes being very close to the theoretical values. The strong performance of the long-wave approximation for small wavenumbers is further demonstrated in figure 14, where we compare the interfacial profiles retrieved from the results of the long-wave and Stokes simulations shown in figure 13. The profiles are plotted at  $t^* = 39.0$ , by which time the dominant mode has taken hold. The agreement is good for  $L/h = 4\pi$  and excellent for  $L/h = 8\pi$ .

Thus far, we have only examined Stokes flows when the initial amplitude is small enough for the linear theory to apply. In figure 15, we show results of two simulations with large initial amplitudes. These calculations were performed with a fixed number of 128 marker points, and a dimensionless time step reduced by the inverse of the linear growth rate of 0.05. Each simulation requires several hours of CPU time on a 2GHz processor. In the first calculation, shown in figure 15(a,b), the capillary number is set to  $Ca = 1.8$ , and the initial amplitude of the interfacial wave is  $|A_1|/h = 0.2$ , the initial amplitude of the surfactant concentration wave is  $|\Gamma_1|/\Gamma_0 = 0.2$ , and the phase shift between the two waves is  $\pi$ . Other flow conditions are described in the figure caption. In this case, the interface amplitude grows before exhibiting a period of decay associated with wave steepening. The interfacial profile is shown on the right

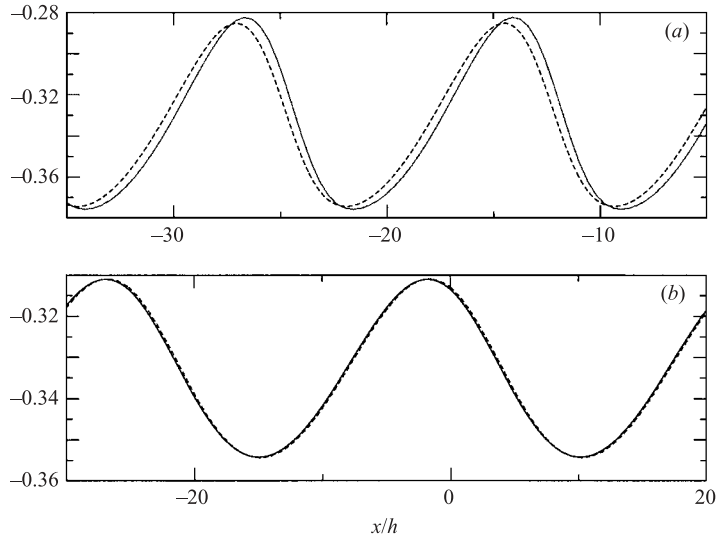


FIGURE 14. Comparison of interfacial wave profiles for Stokes flow (solid lines) and the long-wave approximation (broken lines) for  $h_1/h_2 = 1/2$ ,  $\lambda = 0.5$ ,  $Ca = 0.6$ ,  $Ma = 2$ , and  $\theta_0 = 0$ : (a)  $L/h = 4\pi$  and (b)  $8\pi$ . Both are shown at  $t^* = 39.0$ .

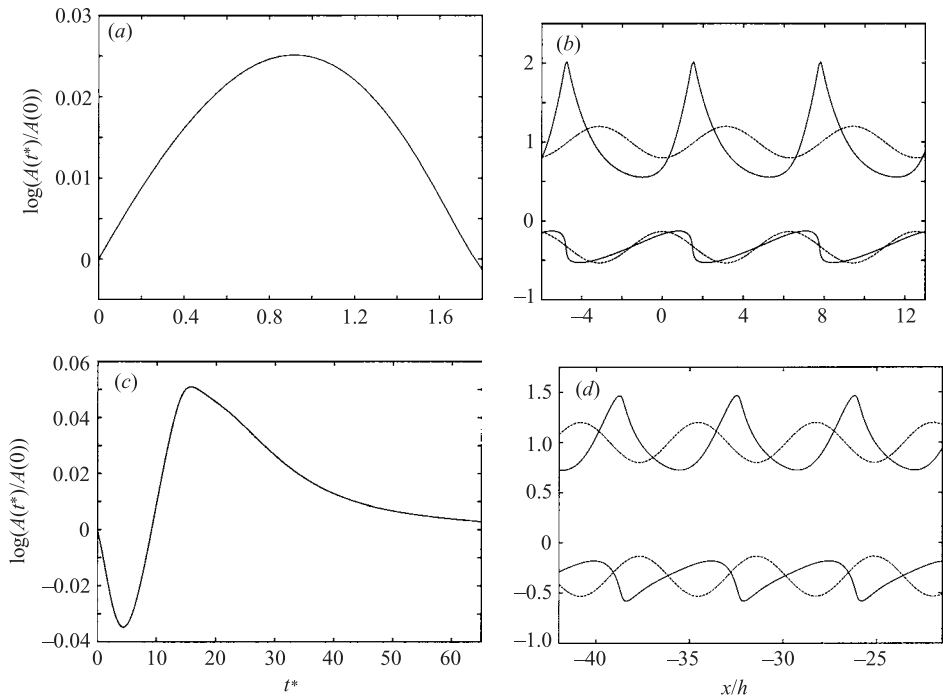


FIGURE 15. Evolution of the interfacial wave in Stokes flow for  $h_1/h_2 = 1/2$ ,  $\lambda = 0.5$ ,  $Ma = 2$ ,  $\theta_0 = 0$ ,  $L/h = 2\pi$ , and (a, b)  $Ca = 1.8$ , (c, d)  $Ca = 0.6$ . In (b, d) the evolving waves (solid lines) are shown together with their initial profiles (broken lines) at dimensionless times (b)  $t^* = 1.7$  and (d)  $t^* = 65.0$ . The upper and lower sets are for the surfactant and interfacial waves respectively.

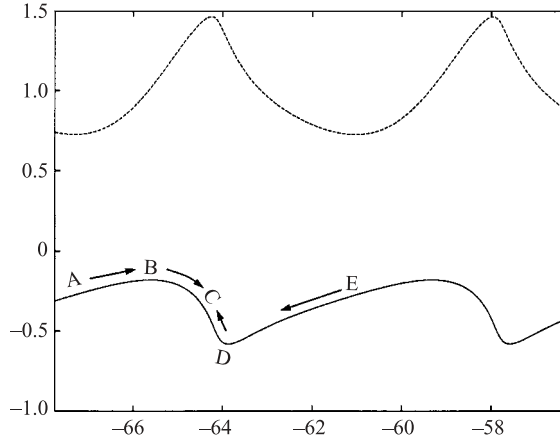


FIGURE 16. Sketch of Marangoni flows along a saturated interfacial wave, shown as a solid line, together with the surfactant concentration wave, shown as a broken line.

just as the wave appears to begin to overturn, at which point the numerics becomes unreliable.

In the second simulation, displayed in figure 15(c,d), the capillary number is  $Ca = 0.6$ , the initial amplitudes are the same as those described for figure 15(a,b), but the phase shift is set to  $0.5932\pi$ . These conditions correspond exactly to those used for the finite-amplitude long-wave calculation discussed earlier (see figure 8). In this case, the wave amplitude decays and then grows before exhibiting a protracted period of slow decay. Although results are shown only up to  $t^* = 65.0$ , there is strong evidence to suggest that the instability saturates. Interestingly, the curve in figure 15(c) approaches zero for large times, meaning that the amplitude of the saturated interfacial wave tends toward that of the initial disturbance. While the shapes of the waves are qualitatively similar to those predicted by the long-wave calculation, the significant difference in size of the saturated amplitude is attributed to the poorer performance of the lubrication approximation at smaller wavenumbers and with the appearance of steep profiles. The saturated waves appear to be robust in the sense that a ‘white-noise’ initial condition consisting of a number of Fourier modes with small, randomly chosen amplitudes also produces nonlinear saturation after a period of linear growth. Nonlinear simulations on extended periodic spatial intervals much larger than those considered here may produce less-ordered non-periodic solutions within those intervals. Such behaviour is known to occur, for example, in the case of the Kuramoto-Sivashinsky equation (e.g. Coward, Papageorgiou & Smyrlis 1995; Wittenberg & Holmes 1999; Halpern & Frenkel 2001). Considerable computational effort would be required to investigate this issue, and it is left as an avenue for future pursuit.

A physical description of the saturated wave may be attempted along the lines of our earlier discussion on the linearly unstable modes. Figure 16 indicates with arrows the Marangoni flow along the saturated wave displayed in figure 15(d). According to the surfactant wave shown above, the surface tension decreases from point A to C and also from point E to C, leading to shear flows in both of these directions. These flows support the wave by feeding fluid toward the steep front at C. It may be noted that a similar qualitative picture applies for figure 15(b). In that case, we surmise that the Marangoni flow toward the counterpart of point C is sufficient to provoke the overturning of the wave.

## 6. Discussion

We have assessed the stability of a flat interface between two viscous layers superposed in two-dimensional channel flow. In the case of a clean interface, instability can only arise at non-zero-Reynolds-numbers. Our analysis confirmed the discovery of Frenkel & Halpern (2002) and Halpern & Frenkel (2003) that the addition of surfactant in the presence of a shear flow introduces unstable modes in both the long-wave and zero-Reynolds-number Stokes limits. The existence and severity of the instability depends upon the values of the Marangoni number, viscosity ratio, and capillary number.

Linear stability analysis based on the long-wave equations conducted with the help of programmed algebraic manipulation produces results that agree well with numerical solutions for sufficiently small disturbance amplitudes. A similar linearized analysis for Stokes flow yields predictions that are in good agreement with boundary-element calculations. For fixed capillary number, we have found that there exists a range of unstable wavenumbers and that this range shrinks as the capillary number is reduced. The effect of viscosity stratification was assessed, and it was found that increasing the viscosity ratio eventually stabilizes the growing mode and suppresses the Marangoni instability. Close inspection of the properties of the normal modes allowed us to describe the physical mechanism underlying the instability, which is in line with intuition. A similar physical argument was given by Frenkel & Halpern (2002).

We have estimated the range of validity of the lubrication model by direct comparison with the results of Stokes flow simulations. The consistency of the two formulations was demonstrated, providing further confidence that the long-wave model is successful in accurately describing the essential features of the instability. For the Stokes-flow calculations, the properties of the normal modes were computed via a linear stability analysis and those for the dominant modes were successfully compared with the output from the boundary-element calculations. The Prony method of exponential curve-fitting was also used to obtain estimates of the recessive modes for comparison with the linearized analysis, but with moderate success. Nonlinear effects were examined for both long-wave and Stokes-flow calculations with disturbances of finite amplitude, and saturation of the instability was observed for particular parameter choices, while the nonlinear features of wave steepening were also captured. The early stages of what appears to be wave overturning were observed in the finite-amplitude calculations. Interfacial waves that grow and saturate due to nonlinear interactions arise in other contexts; two examples are core-annular flow (Joseph *et al.* 1997) and two-layer oscillatory Couette flow (Halpern & Frenkel 2001).

In general, Marangoni tractions arise due to the presence of a surfactant or as the result of thermocapillarity associated with interfacial temperature variations. Previous authors have examined the stability of two-layer channel flow with heated walls, accounting for temperature-dependent viscosity but assuming constant interfacial tension (Pinarbasi & Liakopoulos 1996; Pinarbasi 2002). Linear stability analysis shows that wall temperature differences may stabilize or destabilize the flow depending, among other parameters, on the layer thickness ratio. Assessing the effect of thermocapillarity in this more complicated case is a topic for further investigation.

This research has been supported by a grant provided by the National Science Foundation.

### Appendix A. Linear stability analysis for Stokes flow

In this appendix, we outline the linear stability analysis of the two-layer channel flow in the presence of an insoluble surfactant, in the Stokes flow regime. In carrying out this analysis, it is convenient to work in the inclined system of coordinates shown in figure 1, but shift the origin of the  $y$ -axis so that the unperturbed interface is located at  $y=0$ , the lower wall is located at  $y=-h_1$  and the upper wall is located at  $y=h_2=2h-h_1$ . In the unperturbed configuration, the surfactant concentration is uniform, and the fluids execute unidirectional motion parallel to the channel walls. The  $x$  and  $y$  velocity components, denoted by  $u$  and  $v$ , are given by

$$u_j^{(0)} = -\frac{G + \rho_j g_x}{2\mu_j} y^2 + \xi_j y + u_I, \quad v_j^{(0)} = 0, \quad (\text{A } 1)$$

where  $j = 1, 2$ , respectively, for the lower and upper fluid, the superscript (0) denotes the unperturbed base state,  $G$  is the negative of the axial pressure gradient, and  $u_I$  is the interfacial velocity. To ensure continuity of shear stress at the interface, we require that the interfacial shear rates satisfy  $\xi_1 = \lambda \xi_2$ , where  $\lambda = \mu_2/\mu_1$  is the viscosity ratio. The interfacial velocity and one of  $\xi_1, \xi_2$  are evaluated so that the no-slip boundary condition is satisfied at both walls. The pressure distribution of the base state is given by

$$p_j^{(0)}(y) = -Gx + \rho_j g_y y + P_0, \quad (\text{A } 2)$$

for  $j = 1, 2$ , where  $P_0$  is an inconsequential constant.

A normal-mode perturbation displaces the interface at the position given by the real or imaginary part of  $y = f(x, t) = \epsilon \eta(x, t)$ , where  $\epsilon$  is a dimensionless number whose magnitude is much less than unity,  $\eta(x, t) = A_1 \exp[ik(x - ct)]$  is the normal-mode wave form,  $A_1$  is the complex amplitude of the interfacial wave,  $k = 2\pi/L$  is the wavenumber,  $L$  is the wave length, and  $c$  is the complex phase velocity. Correspondingly, the perturbation stream functions in the lower and upper fluid are given by the biharmonic functions

$$\psi_j^{(1)}(x, y, t) = \epsilon \phi_j(\hat{y}) \exp[ik(x - ct)], \quad (\text{A } 3)$$

where  $\hat{y} = ky$ , and the superscript (1) denotes the disturbance. The modulating functions  $\phi_j(\hat{y})$  are given by

$$\phi_j(\hat{y}) = a_{1j} \cosh \hat{y} + a_{2j} \hat{y} \cosh \hat{y} + a_{3j} \sinh \hat{y} + a_{4j} \hat{y} \sinh \hat{y}, \quad (\text{A } 4)$$

where  $a_{ij}$ , for  $i = 1, 2, 3, 4$ ,  $j = 1, 2$ , are eight complex coefficients. The associated pressure field can be expressed in the form

$$p_j^{(1)}(x, y, t) = \epsilon \mu_j q_j(\hat{y}) \exp[ik(x - ct)], \quad (\text{A } 5)$$

for  $j = 1, 2$ . Substituting this expression into the  $x$  component of the Stokes equation and simplifying, we find

$$q_j(\hat{y}) = ik^2 \left( \frac{d\phi_j}{d\hat{y}} - \frac{d^3\phi_j}{d\hat{y}^3} \right). \quad (\text{A } 6)$$

Kinematic compatibility requires that  $D(y - f)/Dt = 0$ , where  $D/Dt$  is the material derivative. In the linear approximation,

$$\frac{\partial f}{\partial t} + u_I \frac{\partial f}{\partial x} - v^{(1)}(y = 0) = 0. \quad (\text{A } 7)$$

Substituting the preceding expressions, we find

$$A_1 = \zeta a_{11}, \quad (\text{A } 8)$$

where  $\zeta \equiv 1/(c - u_I)$ .

The distribution of the surface surfactant concentration and surface tension are described by the companion functions  $\Gamma(x, t) = \Gamma_0 + \epsilon \Gamma_1 \exp[ik(x - ct)]$  and  $\gamma(x, t) = \gamma_0 + \epsilon \gamma_1 \exp[ik(x - ct)]$ , where  $\Gamma_0, \gamma_0$  are the uniform values corresponding to the flat interface, and  $\Gamma_1, \gamma_1$  are complex amplitudes. Since the perturbations are assumed small, we can write  $\gamma_1 = -Ma\Gamma_1$ , where  $Ma$  is the Marangoni number. The linearized form of the surfactant transport equation is

$$\frac{\partial \Gamma}{\partial t} + u^{(0)} \frac{\partial \Gamma}{\partial x} + \Gamma_0 \left( \frac{\partial u^{(1)}}{\partial x} + \frac{\partial u^{(0)}}{\partial y} \frac{\partial \eta}{\partial x} \right) = D_s \frac{\partial^2 \Gamma}{\partial x^2}, \quad (\text{A } 9)$$

where all terms are evaluated at the unperturbed position,  $y=0$ . Substituting the preceding expressions for the upper fluid velocity, we find

$$\frac{\Gamma_1}{\Gamma_0} = \frac{k(a_{22} + a_{32}) + \xi_2 a_{11} \zeta}{1 + iD_s k \zeta} \zeta. \quad (\text{A } 10)$$

Now, the no-slip and no-penetration conditions at the lower and upper wall require

$$\begin{bmatrix} \cosh \hat{h}_1 & -\hat{h}_1 \cosh \hat{h}_1 & -\sinh \hat{h}_1 & \hat{h}_1 \sinh \hat{h}_1 \\ -\sinh \hat{h}_1 & \cosh \hat{h}_1 + \hat{h}_1 \sinh \hat{h}_1 & \cosh \hat{h}_1 & -\sinh \hat{h}_1 - \hat{h}_1 \cosh \hat{h}_1 \end{bmatrix} \cdot \mathbf{w}_1 = \mathbf{0}, \quad (\text{A } 11)$$

$$\begin{bmatrix} \cosh \hat{h}_2 & \hat{h}_2 \cosh \hat{h}_2 & \sinh \hat{h}_2 & \hat{h}_2 \sinh \hat{h}_2 \\ \sinh \hat{h}_2 & \cosh \hat{h}_2 + \hat{h}_2 \sinh \hat{h}_2 & \cosh \hat{h}_2 & \sinh \hat{h}_2 + \hat{h}_2 \cosh \hat{h}_2 \end{bmatrix} \cdot \mathbf{w}_2 = \mathbf{0}, \quad (\text{A } 12)$$

where  $\mathbf{w}_1 = [a_{11}, a_{21}, a_{31}, a_{41}]^T$ ,  $\mathbf{w}_2 = [a_{12}, a_{22}, a_{32}, a_{42}]^T$ ,  $\hat{h}_1 \equiv kh_1$ , and  $\hat{h}_2 \equiv kh_2$ .

In the linear approximation, continuity of the  $x$  and  $y$  velocity across the interface require, respectively,

$$\zeta(\mathcal{E}_1 - \mathcal{E}_2)a_{11} + a_{21} + a_{31} - a_{22} - a_{32} = 0, \quad a_{11} = a_{12}, \quad (\text{A } 13)$$

where  $\mathcal{E}_j \equiv \xi_j/k$ , for  $j = 1, 2$ , are new coefficients with dimensions of velocity.

The linearized shear stress balance at the interface requires

$$\mu_1 \left( \frac{\partial u}{\partial y} + \frac{\partial v}{\partial x} \right)_{y=0^-} = \mu_2 \left( \frac{\partial u}{\partial y} + \frac{\partial v}{\partial x} \right)_{y=0^+} + (\rho_1 - \rho_2)g_x A_1 + \frac{\partial \gamma}{\partial x}. \quad (\text{A } 14)$$

Substituting the preceding expressions and simplifying, we find

$$(1 - \zeta G_x)a_{11} + a_{41} - \lambda(a_{12} + a_{42}) = i \frac{\gamma_1}{2\mu_1 k}, \quad (\text{A } 15)$$

where we have defined

$$G_x \equiv \frac{(\rho_1 - \rho_2)g_x}{2\mu_1 k^2}. \quad (\text{A } 16)$$

When the channel is horizontal,  $G_x = 0$ . We recall that  $a_{11} = a_{12}$  and  $\gamma_1 = -Ma\Gamma_1$ , and use (A 10) to obtain

$$a_{41} = -a_{12}(1 - \lambda - \zeta G_x) + \lambda a_{42} + \Lambda(a_{22} + a_{32} + \mathcal{E}_2 a_{12} \zeta), \quad (\text{A } 17)$$

where

$$\Lambda \equiv -\frac{iMa\gamma_0 \zeta}{2\mu_1(1 + iD_s k \zeta)} \quad (\text{A } 18)$$

is a dimensionless complex group. In the absence of a surfactant,  $\Lambda = 0$ .

The linear normal stress balance at the interface requires

$$\left( -\mu_1 q_1 + \mu_2 q_2 - 2ik^2 \mu_1 \frac{d\phi_1}{d\hat{y}} + 2ik^2 \mu_2 \frac{d\phi_2}{d\hat{y}} \right)_{y=0} - (\rho_1 - \rho_2) g_y A_1 = -\gamma_0 A_1 k^2. \quad (\text{A } 19)$$

Substituting  $q_j(y=0) = -2ik^2 a_{2j}$ , simplifying, and using (A 8), we find

$$a_{31} = \lambda a_{32} - i\Pi \zeta a_{12}, \quad (\text{A } 20)$$

where

$$\Pi \equiv \frac{1}{2\mu_1} \left[ \gamma_0 - \frac{(\rho_1 - \rho_2) g_y}{k^2} \right] = \frac{\gamma_0}{2\mu_1} - G_y \quad (\text{A } 21)$$

is a property group with dimensions of velocity, and we have defined

$$G_y \equiv \frac{(\rho_1 - \rho_2) g_y}{2\mu_1 k^2}. \quad (\text{A } 22)$$

To formulate the eigenvalue problem, we substitute (A 20) into (A 13), and rearrange to find

$$a_{21} = \zeta(i\Pi + \mathcal{E}_2 - \mathcal{E}_1) a_{12} + a_{22} + (1 - \lambda) a_{32}. \quad (\text{A } 23)$$

Finally, we substitute (A 17), (A 20), and (A 23) into the linear system (A 11), and obtain the equivalent system

$$\begin{bmatrix} C_{11} - \zeta(C_{12} + \Lambda C_{13}) & \hat{h}_1(\Lambda \sinh \hat{h}_1 - \cosh \hat{h}_1) \\ C_{21} + \zeta(C_{22} + \Lambda C_{23}) & (1 - \Lambda \hat{h}_1) \cosh \hat{h}_1 + (\hat{h}_1 - \Lambda) \sinh \hat{h}_1 \\ \frac{(\lambda - 1)\hat{h}_1 \cosh \hat{h}_1 + (\Lambda \hat{h}_1 - \lambda) \sinh \hat{h}_1}{(1 - \Lambda \hat{h}_1) \cosh \hat{h}_1 - (\Lambda + (\lambda - 1)\hat{h}_1) \sinh \hat{h}_1} & \frac{\lambda \hat{h}_1 \sinh \hat{h}_1}{-\lambda(\sinh \hat{h}_1 + \hat{h}_1 \cosh \hat{h}_1)} \end{bmatrix} \cdot \mathbf{w}_2 = \mathbf{0}, \quad (\text{A } 24)$$

where

$$\left. \begin{aligned} C_{11} &\equiv \cosh \hat{h}_1 - (1 - \lambda) \hat{h}_1 \sinh \hat{h}_1, \\ C_{12} &\equiv [\hat{h}_1 \cosh \hat{h}_1 (\mathcal{E}_2 - \mathcal{E}_1) - G_x \hat{h}_1 \sinh \hat{h}_1] + i\Pi (\hat{h}_1 \cosh \hat{h}_1 - \sinh \hat{h}_1), \\ C_{13} &\equiv \hat{h}_1 \mathcal{E}_2 \sinh \hat{h}_1, \\ C_{21} &\equiv -\sinh \hat{h}_1 + (1 - \lambda) (\sinh \hat{h}_1 + \hat{h}_1 \cosh \hat{h}_1), \\ C_{22} &\equiv [(\cosh \hat{h}_1 + \hat{h}_1 \sinh \hat{h}_1) (\mathcal{E}_2 - \mathcal{E}_1) - G_x (\sinh \hat{h}_1 + \hat{h}_1 \cosh \hat{h}_1)] + i\Pi \hat{h}_1 \sinh \hat{h}_1 \\ C_{23} &\equiv -\mathcal{E}_2 (\sinh \hat{h}_1 + \hat{h}_1 \cosh \hat{h}_1). \end{aligned} \right\} \quad (\text{A } 25)$$

Appending (A 24) to (A 12), we obtain the homogeneous system  $\mathbf{M} \cdot \mathbf{w}_2 = \mathbf{0}$ , where  $\mathbf{M}$  is an obvious  $4 \times 4$  complex coefficient matrix. Setting the determinant of  $\mathbf{M}$  to zero provides us with a quadratic equation for the complex phase velocity  $c$ , corresponding to two normal modes. In the event of equal-density fluids and zero surfactant diffusivity, this equation coincides exactly with equation (3.19) of Halpern & Frenkel (2003).

A typical calculation with equal fluid densities and varying surfactant diffusivity is shown in figure 17, where the dominant dimensionless growth rate  $s$  defined in §3 is plotted against the inverse of the Péclet number  $\alpha = 1/Pe$ . As  $\alpha$  increases, eventually surfactant diffusion dominates convection, and the concentration over the

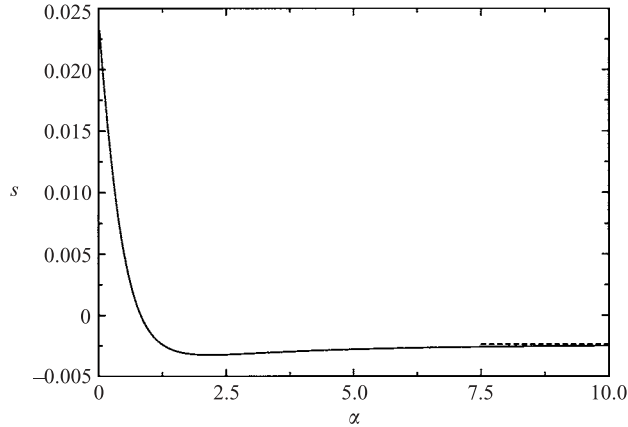


FIGURE 17. Effect of the surfactant diffusivity on the dominant growth rate for  $h_1/h_2 = 1/2$ ,  $\lambda = 0.5$ ,  $Ca = 0.6$ ,  $Ma = 2.0$ , and  $\theta_0 = 0$ . The dashed line shows the value for a clean interface,  $-0.00239$ .

interface tends to become uniform. The dominant growth rate approaches the value  $-0.00239$  for a surfactant-free interface, shown as a broken line in the figure; the second growth rate, not shown in the figure, asymptotes toward  $-(h^3 \mu_1 \xi_1 / \gamma_0) k^2 \alpha$ . Thus, in the limit  $\alpha \rightarrow \infty$ , the dynamics reduces to that for a clean interface with uniform surface tension.

### Appendix B. Boundary-element formulation

In this appendix, we outline the boundary-integral formulation of the two-fluid channel flow discussed in §2, and describe a boundary-element method of solution. To develop the integral formulation, we decompose the velocity field in each fluid into a reference component denoted by the superscript  $R$ , and a disturbance component denoted by the superscript  $D$ , so that  $\mathbf{u}^{(j)} = \mathbf{u}^{R(j)} + \mathbf{u}^{D(j)}$ , for  $j = 1, 2$ , where the superscripts (1) and (2) denote, respectively, the lower and upper fluid. The pressure and stress are decomposed in a similar fashion. The reference velocity is chosen to be

$$u_x^{R(j)} = \frac{\chi + \rho_j g_x}{2\mu_j} (h^2 - y^2) + \xi(y - y_R), \quad u_y^{R(j)} = 0, \quad (\text{B } 1)$$

where

$$\xi = \frac{U_2 - U_1}{2h}, \quad y_R = -h \frac{U_2 + U_1}{U_2 - U_1}, \quad (\text{B } 2)$$

and  $\chi$  is the negative of a specified axial pressure gradient. The corresponding pressure field is given by

$$p^{R(j)} = -\chi x + \rho_j g_y y + P_j, \quad (\text{B } 3)$$

where  $g_y$  is the  $y$  component of the acceleration due to gravity, and  $P_j$  are constants. The disturbance velocity and pressure satisfy the Stokes flow equations (5.1) with the body force excluded. Since the reference velocity satisfies the no-slip boundary condition at the channel walls, the disturbance velocity is required to vanish over both walls.

Working in the manner described by Pozrikidis (1997a, 1998a), under the stipulation that the disturbance flow does not induce a pressure drop across each period, we

derive the following Fredholm integral equation of the second kind for the interfacial velocity:

$$\begin{aligned}
 u_j^{D(1)}(\mathbf{x}_0) = & -\frac{\lambda}{1+\lambda} \Delta u_j^R(\mathbf{x}_0) - \frac{1}{2\pi\mu_1} \frac{1}{1+\lambda} \int_I G_{ij}(\mathbf{x}, \mathbf{x}_0) \Delta f_i^D(\mathbf{x}) d\mathbf{l}(\mathbf{x}), \\
 & + \frac{1}{2\pi} \frac{1-\lambda}{1+\lambda} \int^{PV} u_i^{D(1)}(\mathbf{x}) T_{ijk}(\mathbf{x}, \mathbf{x}_0) n_k(\mathbf{x}) d\mathbf{l}(\mathbf{x}) \\
 & - \frac{1}{2\pi} \frac{\lambda}{1+\lambda} \int^{PV} (u_i^{R(1)} - u_i^{R(2)})(\mathbf{x}) T_{ijk}(\mathbf{x}, \mathbf{x}_0) n_k(\mathbf{x}) d\mathbf{l}(\mathbf{x}), \quad (\text{B } 4)
 \end{aligned}$$

where  $I$  is one period of the interface,  $G_{ij}$  is the periodic Green's function for channel flow, and  $T_{ijk}$  its associated stress tensor, and  $PV$  signifies the principal value of the double-layer potential. The strength density of the single-layer potential over the interface is given by  $\Delta \mathbf{f}^D = \Delta \mathbf{f} - \Delta \mathbf{f}^R$ , where the traction discontinuity  $\Delta \mathbf{f}$  is given in (5.2), and the discontinuity of the reference flow is given by

$$\begin{aligned}
 \Delta \mathbf{f}^R & \equiv (\boldsymbol{\sigma}^{R(1)} - \boldsymbol{\sigma}^{R(2)}) \cdot \mathbf{n} \\
 & = \left[ \begin{array}{c|c} -\Delta \rho g_y y_R & \mu_1(1-\lambda)\xi - \Delta \rho g_x y_R \\ \mu_1(1-\lambda)\xi - \Delta \rho g_x y_R & -\Delta \rho g_y y_R \end{array} \right] \cdot \mathbf{n} - (P_1 - P_2)\mathbf{n}, \quad (\text{B } 5)
 \end{aligned}$$

with  $\Delta \rho = \rho_1 - \rho_2 = \rho_1(1 - \delta)$ .

The solution of the integral equation can be found efficiently using the boundary-element method (e.g. Pozrikidis 2002). In the present implementation, one period of the interface is discretized into a sequence of straight boundary elements over which the flow variables are approximated by uniform functions. Boundary collocation is applied then to obtain a system of linear equations for the disturbance velocities over each element. The solution to this system is used to advance in time the position of the nodes defining the interfacial elements, using Runge–Kutta integration.

The convection–diffusion equation for the surfactant (2.3) is treated simultaneously using a finite-volume method (Yon & Pozrikidis 1998), wherein the interface is described by the same set of boundary elements. The resulting ordinary differential equations are integrated in time using an implicit method. The accuracy of the computations was checked by implementing a separate scheme due to Ni (1982), which is second-order accurate in both the temporal and spatial step.

## REFERENCES

- ADAMSON, A. W. 1990 *Physical Chemistry of Surfaces*. Wiley.
- COWARD, A. V., PAPAGEORGIOU, D. T. & SMYRLIS, Y. S. 1995 Nonlinear stability of oscillatory core-annular flow: a generalized Kuramoto-Sivashinsky equation with time period coefficients. *Z. angew Math. Phys.* **46**, 1–39.
- FRENKEL, A. L. & HALPERN, D. 2002 Stokes-flow instability due to interfacial surfactant. *Phys. Fluids* **14**, 45–48.
- HALPERN, D. & FRENKEL, A. L. 2001 Saturated Rayleigh-Taylor instability of an oscillating Couette film flow. *J. Fluid Mech.* **446**, 67–93.
- HALPERN, D. & FRENKEL, A. L. 2003 Destabilization of a creeping flow by interfacial surfactant: Linear theory extended to all wavenumbers. *J. Fluid Mech.* **485**, 191–220.
- HESLA, T. I., PRANCKH, F. R. & PREZIOSI, L. 1986 Squire's theorem for two stratified fluids. *Phys. Fluids* **29**, 2808–2811.
- HILDEBRAND, F. B. 1974 *Introduction to Numerical Analysis*. Dover.
- Ji, W. & SETTERWALL, F. 1994 On the instabilities of vertical falling liquid films in the presence of surface-active solute. *J. Fluid Mech.* **278**, 297–323.

- JOSEPH, D. D., BAI, R., CHEN, K. P. & RENARDY, Y. Y. 1997 Core-annular flows. *Annu. Rev Fluid Mech.* **29**, 65–90.
- KAY, S. M. & MARPLE, S. L. 1981 Spectrum analysis – a modern perspective. *Proc. IEEE* **69**, 1380–1419.
- LI, X. & POZRIKIDIS, C. 1997 The effect of surfactants on drop deformation and on the rheology of dilute emulsions in Stokes flow. *J. Fluid Mech.* **341**, 165–194.
- MARPLE, S. L. 1987 *Digital Spectral Analysis with Applications*. Prentice Hall.
- NI, R.-H. 1982 A multiple-grid scheme for solving the Euler equations. *AIAA J.* **20**, 1565–1571.
- OOMS, G., SEGAL, A., CHEUNG, S. Y. & OLIEMANS, R. V. A. 1985 Propagation of long waves of finite amplitude at the interface of two viscous fluids. *Intl J. Multiphase Flow* **11**, 481–502.
- PINARBASI, A. 2002 Interface stabilization in two-layer channel flow by surface heating or cooling. *Eur. J. Mech. B/Fluids* **21**, 225–236.
- PINARBASI, A. & LIAKOPOULOS, A. 1996 On the influence of temperature and viscosity fluctuations on interfacial instability. *Intl Commun. Heat Mass Transfer* **23**, 485–493.
- POZRIKIDIS, C. 1992 *Boundary Integral and Singularity Methods for Linearized Viscous Flow*. Cambridge University Press.
- POZRIKIDIS, C. 1997a Instability of two-layer creeping flow in a channel with parallel-sided walls. *J. Fluid Mech.* **351**, 139–165.
- POZRIKIDIS, C. 1997b *Introduction to Theoretical and Computational Fluid Dynamics*. Oxford University Press.
- POZRIKIDIS, C. 1998a Gravity-driven flow of two adjacent layers through a channel and down a plane wall. *J. Fluid Mech.* **371**, 345–376.
- POZRIKIDIS, C. 1998b Multi-film flow down an inclined plane: Simulations based on the lubrication approximation, and normal-mode decomposition of linear waves. In *Fluid Dynamics at Interfaces* (ed. W. Shyy & R. Narayanan) Cambridge University Press.
- POZRIKIDIS, C. 2002 *A Practical Guide to Boundary Element Methods with the Software Library BEMLIB*. Chapman & Hall/CRC Press.
- POZRIKIDIS, C. 2003 Effect of surfactants on film flow down a periodic wall. *J. Fluid Mech.* **496**, 105–127.
- POZRIKIDIS, C. 2004 Instability of multi-layer channel and film flows. *Adv. Appl. Mech.*, In press.
- THAOKAR, R. M. & KUMARAN, V. 2002 Stability of fluid flow past a membrane. *J. Fluid Mech.* **472**, 29–50.
- TREFETHEN, L. N., TREFETHEN A. E., REDDY, S. C. & DRISCOLL, T. A. 1993 Hydrodynamic stability without eigenvalues. *Science* **261**, 578–584.
- WITTENBER, R. & HOLMES, P. 1999 Scale and space localization in the Kuramoto-Sivashinsky equation. *Chaos* **9**, 452–465.
- WONG, H., RUMSCHITZKI, D. & MALDARELLI, C. 1996 On the surfactant mass balance at a deforming fluid interface. *Phys. Fluids* **8**, 3203–3204.
- YIH, C. S. 1967 Instability due to viscosity stratification. *J. Fluid Mech.* **27**, 337–352.
- YON, S. & POZRIKIDIS, C. 1998 A finite-volume/boundary-element method for flow past interfaces in the presence of surfactants, with application to shear flow past a viscous drop. *Computers Fluids* **27**, 879–902.